ORIGINAL ARTICLE

Numerical simulation of sand dune erosion

**A. M. G. Lopes · L. A. Oliveira ·
Almerindo D. Ferreira · J. P. Pinto**

Abstract Erosion of sand or other granular material is a subject of utmost importance in several fields of practical interest, including industrial processes or environmental issues. Resulting from intricate interaction between the incident flow field and localized body forces responsible for the granular material cohesion, erosion is a particularly complex phenomenon. The present work addresses this problem, proposing a numerical method to compute the time evolution of a sand dune subjected to aeolian erosion, along with the associated entrainment and deposition fluxes. Turbulent fluid flow is computed through a three-dimensional Navier-Stokes solver based on a generalized coordinate system. A Lagrangian approach is adopted for tracking the trajectories of particles entrained in the saltation regime, thus allowing prediction of the corresponding deposition locations. Different models for saltation fluxes are tested, along with several formulations for the creeping-to-saltation flux ratio, creeping threshold and creeping distance. Comparison with results from wind tunnel experiments is very encouraging, stressing the relative importance of creeping in the erosion process for the presently studied conditions.

1 Introduction

Numerical modeling of two-phase flows has been increasingly used as an efficient and relatively affordable support to design and optimization in industry as well as for environmental protection (cf. [1–4]). In particular, the transport of solid particles by atmospheric wind is present in many situations of practical relevance: dune formation and erosion; transport of dust generated from different sources, e.g. through the wind action on coal storage piles.

A. M. G. Lopes (✉) · L. A. Oliveira · A. D. Ferreira · J. P. Pinto
ADAI-LAETA, Department of Mechanical Engineering, University of Coimbra,
3030-788 Coimbra, Portugal
e-mail: antonio.gameiro@dem.uc.pt

When a dune or stockpile, consisting of cohesionless grains, is exposed to a sufficiently strong wind, its profile is susceptible of being reshaped as a result of entrainment and deposition of particles. The dynamics of such a phenomenon depends on a variety of factors, including the flow strength and direction relative to the dune, surrounding conditions and sediment supply.

The dynamics of particles exposed to the wind is a complex function of several parameters, which can be subdivided in two main groups: particles' properties and flow characteristics. In the first group, one can name the size of particles and granular material density. The second group includes fluid properties (e.g., fluid density, ρ, and viscosity, μ), and flow characteristics, namely the wall shear stress, τ_w, or, correspondingly, the friction velocity, defined as $u_* = \sqrt{\tau_w/\rho}$.

According to the pioneering work of Bagnold [5], the elementary dynamics of relatively large sand grains, subjected to an incident fluid flow, consists of saltation and creeping. Saltation is the process in which sand grains make short jumps, while creeping is the process where relatively large particles, of diameter in the range of 0.5–1 mm, roll or slide along the free surface. Saltation is often considered to be the primary mode of aeolian transport; however creeping flux becomes significant if the sand grains are relatively large.

Different strategies have been adopted to model the evolution of dunes morphology. In the cellular automata dune model (e.g., [6–9]), the eroded slabs are chosen randomly and moved downwind a specified number of lattices.

Some other works (e.g., [10–12]) are based on the mass conservation equation of Exner [13], by balancing the temporal variation of sand surface elevation with the divergence of the saltation sand flux. The use of this procedure requires the adoption of the saturation length concept [14].

For relatively gentle dunes, and assuming that flow separation does not occur, some researchers have used the analytic theory of boundary layer perturbation of Jackson and Hunt [15] to prescribe the shear stress (e.g., [10,12]).

In most of the aforementioned studies, only the saltation process was modeled, and creeping was assumed negligible. In the present work, the creeping flux is expected to be quite significant due to the sand granulometry, dune surface shape and associated flow conditions. This is in agreement with visual observations during the experiments. Therefore, creeping has to be modeled in conjunction with saltation in the present case. Three saltation models (proposed, respectively, by Bagnold [5], Kawamura [16], and Lettau and Lettau [17]) are tested in the case of a sinus-shaped sand dune, and the model of Wang and Zheng [18] is adopted for the creeping. Those flux models were obtained through field observation and wind tunnel experiments for flat, horizontal sand bed conditions, and their constants of proportionality were tuned for those conditions. As the original sand surface geometry considered in the present study is not flat, but instead presents a sinusoidal shape, the models' parameters require appropriate calibration, which is accomplished by fitting the computational results to the experimental data of Ferreira and Fino [19], with recourse to calibration coefficients to be defined later.

In this work, sand erosion predictions are established through the use of a computational model coupling the fluid phase calculation (CFD) with the particle phase (erosion) calculation, via a time-marching procedure. The CFD model is a home-made code that solves the three-dimensional Reynolds-averaged Navier–Stokes equations in a boundary fitted coordinate system, using a control volume approach. Turbulence effects upon the mean flow field are simulated with a $k - \varepsilon$ type turbulence model. The resulting solution provides the shear stress distribution along the sandy surface, which is necessary to determine the emission fluxes due to saltation and creeping processes. The flow field obtained from the CFD model also

provides the required information to compute the Lagrangian tracking of particle saltation trajectories. Distances covered by those particles which are entrained along the dune surface due to creeping are computed with a specific model. In order to simulate the avalanche process, the maximum slope between adjacent nodes is enforced to 33°, the angle of repose. As reported later, the time evolution of the dune morphology is calculated through an iterative procedure, where the global duration is divided into a number of successive time steps: in each of these parcels, flow and particulate phases are calculated separately, and the dune shape is then correspondingly updated, as a consequence of combined erosion and deposition effects.

Results indicate that, for the present conditions, the relative importance of creeping, as compared to saltation, in the global erosion phenomenon, clearly exceeds the one predicted by most authors for flat, horizontal sand beds.

2 Models

2.1 Flow simulation

2.1.1 Governing equations

The partial differential equations that govern the steady three-dimensional turbulent wind flow and related phenomena occurring in this problem can be obtained as particular cases of the following general differential equation, written for a unit volume in the conservative form and in Cartesian co-ordinates, x_i, for i ranging from 1 to 3 [20]:

$$\frac{\partial}{\partial x_i}\left(\rho u_i \phi - \Gamma_{eff,\phi}\frac{\partial \phi}{\partial x_i}\right) = S_\phi \tag{1}$$

where ρ is the air density, which is assumed to be constant, and the Einstein convention is adopted for the index i. In Eq. (1), where the first term inside the brackets accounts for advection, ϕ is a general specific (per unit mass) time-mean dependent variable, to which are associated particular values or expressions for the corresponding effective diffusion coefficient, $\Gamma_{eff,\phi}$, and source term, S_ϕ, as follows:

Conservation of momentum ($\phi \equiv u_i$)

$$\rho\frac{\partial}{\partial x_j}\left(u_i u_j\right) = -\frac{\partial p}{\partial x_i} + \frac{\partial}{\partial x_j}\left[\Gamma\left(2\frac{\partial u_i}{\partial x_j}\right)\right] + \frac{\partial}{\partial x_j}\left[\Gamma\left(\frac{\partial u_i}{\partial x_j}+\frac{\partial u_j}{\partial x_i}\right)\right] - \frac{2}{3}\rho\frac{\partial k}{\partial x_i} \tag{2}$$

where p stands for pressure and $\Gamma = \mu + \mu_t$, with μ and μ_t being the laminar and the turbulent dynamic viscosity, respectively.

Conservation of mass ($\phi \equiv 1$)

$$\frac{\partial u_i}{\partial x_i} = 0 \tag{3}$$

Turbulence modelling ($\phi \equiv k, \varepsilon$)

Turbulence effects upon the mean flow field are modeled with recourse to the standard $k - \varepsilon$ turbulence model of Launder and Spalding [21]. The corresponding equations are presented below.

$$\frac{\partial}{\partial x_i}(\rho u_i k) = \frac{\partial}{\partial x_i}\left[\left(\mu + \frac{\mu_t}{\sigma_k}\right)\frac{\partial k}{\partial x_i}\right] + P_1 - \rho\varepsilon \tag{4}$$

$$\frac{\partial}{\partial x_i}(\rho u_i \varepsilon) = \frac{\partial}{\partial x_i}\left[\left(\mu + \frac{\mu_t}{\sigma_\varepsilon}\right)\frac{\partial \varepsilon}{\partial x_i}\right] + \frac{\varepsilon}{K}(C_1 P_1 - C_2\rho\varepsilon) \tag{5}$$

$$P_1 = -\rho\overline{u_i' u_j'}\frac{\partial u_i}{\partial x_j} \tag{6}$$

$$\mu_t = C_\mu\frac{\rho k^2}{\varepsilon} \tag{7}$$

$$C_\mu = 0.033; \quad C_1 = 1.45; \quad C_2 = 1.9; \quad \sigma_k = 1; \quad \sigma_\varepsilon = 1.3 \tag{8}$$

2.1.2 Physical treatment near solid boundaries

Roughness effects upon the boundary layer are modeled by assigning a variation of velocity near the ground according to the following logarithmic law:

$$\frac{u_1 u_*}{\tau_w/\rho} = \frac{1}{\kappa}\ln\left(E\frac{\rho u_* z_1}{\mu}\right) - \Delta B \tag{9}$$

where κ is the von Karman constant (=0.41), u_1 is the velocity at the distance z_1 from the ground and u_* represents the friction velocity. ΔB accounts for the shift intercept of the logarithmic law at $z = 0$ due to roughness effects. For uniform sand-type roughness, ΔB is strongly correlated with the non-dimensional roughness height, K_s^+:

$$K_s^+ = \rho K_s\, u_*/\mu \tag{10}$$

where K_s is the average value of the physical roughness height. According to Cecebi and Bradshaw [22], ΔB assumes different formulations depending on the flow regime, as described next.

Hydrodynamically smooth regime $(K_s^+ \leq 2.25)$

$$\Delta B = 0 \tag{11}$$

Transitional regime $(2.25 < K_s^+ \leq 90)$

$$\Delta B = \frac{1}{\kappa}\ln\left(\frac{K_s^+ - 2.25}{87.75} + 0.5K_s^+\right)\sin\left[0.4258\left(\ln K_s^+ - 0.811\right)\right] \tag{12}$$

Fully rough regime $(K_s^+ > 90)$

$$\Delta B = \frac{1}{\kappa}\ln(1 + 0.5K_s^+) \tag{13}$$

The logarithmic law for wind speed is based on the hypothesis of local equilibrium, i.e., shear stress τ_w is constant with height and turbulence kinetic energy production rate equals the dissipation rate. This may be stated as:

$$\varepsilon = \frac{P_1}{\rho} = \frac{\tau_w}{\rho}\frac{\partial u}{\partial z} = \frac{\tau_w^2}{\mu_t \rho} \tag{14}$$

Substituting Eq. (7) into Eq. (14), and noting that $\tau_w = \rho u_*^2$, leads to:

$$u_* = C_\mu^{1/4}\sqrt{k} \tag{15}$$

The shear stress at the ground is computed from Eq. (9):

$$\tau_w = \frac{\rho u_p \, u_*}{\left[\frac{1}{\kappa} \ln \left(E \frac{\rho u_* z_p}{\mu}\right) - \Delta B\right]} \tag{16}$$

where the friction velocity, u_*, is given by (15). This evaluates the momentum flux at the ground, thus providing the corresponding boundary condition. The value for the turbulence kinetic energy at the solid boundary is directly given by Eq. (15):

$$k = \frac{u_*^2}{\sqrt{C_\mu}} \tag{17}$$

and, for the dissipation rate:

$$\varepsilon = \frac{u_*^3}{\kappa d} \tag{18}$$

2.1.3 Transformation of the governing equations and their numerical solution

In order to deal with irregular boundary geometries, the original transport equations are transformed from the Cartesian space into a generalized coordinate system, through the application of the chain rule, and recast in the strong law conservation form. Exemplifying for the momentum conservation, the following formulation is obtained:

$$\frac{\partial}{\partial \xi_j} \left(J\rho U_j u_i\right) = \frac{\partial}{\partial \xi_m} \mu_{eff} J \left[g^{mn} \frac{\partial u_i}{\partial \xi_n} + \frac{\partial \xi_m}{\partial x_j} \frac{\partial \xi_n}{\partial x_i} \frac{\partial u_j}{\partial \xi_n} - \frac{2}{3} \frac{\partial \xi_m}{\partial x_i} \frac{\partial \xi_n}{\partial x_j} \frac{\partial u_j}{\partial \xi_n}\right]$$
$$- J \frac{\partial \xi_j}{\partial x_i} \frac{\partial p}{\partial \xi_j} - \frac{2}{3} J \left(\frac{\partial \xi_j}{\partial x_i} \frac{\partial (\rho k)}{\partial \xi_j}\right) \tag{19}$$

where u_i is a generic Cartesian velocity component, x_i and ξ_i are the generic Cartesian and computational coordinates, respectively, U_i is a generic contravariant velocity component, the terms g^{mn} are contravariant metric relations and J is the Jacobian of the transformation. A control volume (CV) approach is used for the numerical integration of the transport equations. A staggered grid is adopted for the location of the three components of the velocity vector, which are located at the centre of each face of each CV. Scalars such as pressure and turbulent quantities are positioned at the geometric centre of the CV's. After discretisation and integration, the equations are cast in the general algebraic form [20]:

$$a_P \phi_P \left(1 + \frac{1}{E}\right) = \sum_{nb} a_{nb} \phi_{nb} + b + \frac{a_P \phi_P^*}{E} \tag{20}$$

This equation relates the value of the generic variable ϕ (velocity components or turbulence quantities) at location P with its neighbouring (nb) values. b is a source term and E represents a subrelaxation parameter. The SIMPLEC algorithm [23], adapted for a generalized coordinate system (cf. [24], for details), is employed to obtain the segregated solution of the primitive Cartesian velocity components (u, v, w) and pressure, p. The discretized equations are then solved using the tridiagonal matrix algorithm TDMA [20], with sweeps of the whole domain along the three computational directions.

2.2 Particle tracking

Numerical simulation of the present two-phase flow problem is performed by adopting an Eulerian type description for the continuous phase (as described in the preceding sections), together with a Lagrangian type approach for tracking the particle trajectories. The latter type of analysis was also adopted by other authors for horizontal bed configurations, namely Anderson and Haff [25] and Shao and Li [26]. As reported by Oliveira et al. [27], the solid phase (sand grains) is considered to be composed of hard, spherical, non-rotating, smooth, elastic particles of uniform diameter d^p, mass m^p and mass density ρ^p, where the superscript, ^{p}, stands for particulate phase. Owing to the very low value of the air-to-sand mass density ratio, ρ/ρ^p, the only significant forces acting upon each particle are assumed to be the drag and gravitational forces. The equation of motion for a single sand particle of unit mass is therefore reduced to the following, simplified form [28]:

$$\frac{du_i^p}{dt} = \frac{3}{4}\frac{\mu}{\rho^p(d^p)^2}C_D\text{Re}^p(u_i - u_i^p) + g_i\left(1 - \frac{\rho}{\rho^p}\right) \qquad (21)$$

where t and g_i stand for time and gravity acceleration along direction i, respectively, and the two terms in the right-hand side represent, in the same order, the forces that were mentioned above and are responsible for the particle acceleration (left-hand side). In Eq. (21), the particle Reynolds number, Re^p, is based on the particle-to-fluid relative velocity, $\left|\vec{V}^{rel}\right| = \sqrt{\left(u_i - u_i^p\right)^2}$, and its product with the drag coefficient, C_D, is calculated using an empirical relation reported by Wallis [29]:

$$C_D\text{Re}^p = \begin{cases} 24 + 3.6\,(\text{Re}^p)^{0.687}, & (\text{Re}^p \leq 1000) \\ 0.44\text{Re}^p, & (\text{Re}^p > 1000) \end{cases} \qquad (22)$$

The particle trajectories, x_i^p, are related to their instantaneous velocities, u_i^p, through the following expression:

$$\frac{dx_i^p}{dt} = u_i^p \qquad (23)$$

The position and velocity of each particle along its trajectory are calculated for a time level, $t + \Delta t$, as functions of the corresponding values that are available for the previous time level, t. Eqs. (21) and (23) can be solved analytically, provided the time step Δt is small enough, so that the properties of the fluid phase may be considered essentially constant between the instants t and $t + \Delta t$. As an alternative for those cases where the fluid properties cannot be considered unchanged over the integration time interval, Δt, the present model also includes a fourth-order Runge-Kutta numerical integration scheme. The selection of the time step, Δt, is based upon the local value of the Stokes number, $St = \tau^p/\tau$, where τ^p and τ are the characteristic particle and fluid response times, respectively. In practice, if $St << 1$, the particle essentially follows the fluid flow, and the time step is taken as $\Delta t = \tau$; if $St \approx 1$ or $St >> 1$, then $\Delta t = \tau^p$. In any case, Δt should not significantly exceed the time necessary for the particle to traverse the local Eulerian grid cell. A further restriction is imposed for those cases where the Runge-Kutta method is used: Δt should always be kept below the stability limit that applies to this explicit type method. The details for the integration procedure may be found in [27] and [30].

The interactions of the particles with solid boundaries are modeled through collisions with the introduction of a restitution coefficient. For each particle, the trajectory calculation

is terminated when the particle leaves the calculation domain at outflow boundaries, or, alternatively, its position remains unchanged after a significant amount of time.

In this work, the effect of fluid turbulence upon particle dispersion is accounted for by using the concept of particle-eddy encounters [27,31].

2.3 Sand erosion simulation

Along its own trajectory, each particle of mass m^p is actually representative of a number of identical particles that are permanently injected into the calculation domain, with constant emission flux, through the same injection point. Each trajectory is thus associated to a mass flow rate of particles, q. In the present conditions, the phenomenon which is responsible for the injection of sand particles into the flow domain is ground erosion due to the wind. The two mechanisms considered here that originate erosion are saltation (sand grains are airborne) and creeping (grains roll over the surface).

Many different models are available in the literature, relating the local wind characteristics with the resulting wind erosion by saltation (see [32] for a review). The great majority of such proposals is based upon a relation between the local value of the friction velocity, u_*, and the corresponding threshold value, $u_{*t,salt}$, below which no saltation occurs. In the present work, the following three models (hereafter called BG, KW and LL) are tested for the saltation flux, q_{salt}:

$$q_{salt,BG} = c_{BG} \sqrt{\frac{d^p}{D}} \frac{\rho}{g} u_* \left(u_*^2 - u_{*t,salt}^2\right) \tag{24}$$

$$q_{salt,KW} = c_{KW} \frac{\rho}{g} \left(u_* - u_{*t,salt}\right) \left(u_* + u_{*t,salt}\right)^2 \tag{25}$$

$$q_{salt,LL} = c_{LL} \sqrt{\frac{d^p}{D}} \frac{\rho}{g} u_*^2 \left(u_* - u_{*t,salt}\right) \tag{26}$$

Equation (24) is a straightforward modification of Bagnold's original model [5,33], and the other two were proposed by Kawamura [16], and Lettau and Lettau [17], respectively. In Eqs. (24) and (26), d^p is the grain diameter ($d^p = 0.5$ mm in the present work, according to [34]), D is a reference sand grain diameter ($D = 0.25$ mm, regardless of the value of d^p, see [5]). Constants c_{BG}, c_{KW}, and c_{LT} were determined empirically for flat, horizontal surfaces. Corresponding values, from original references, are $c_{BG} = 1.8$, $c_{KW} = 2.78$ and $c_{LL} = 4.2$. These values were, in the present work, adapted to better fit the experimental data (which includes inclined surfaces). Best fit (results to be presented later in this work) was obtained using $c_{BG} = 4.066$, $c_{KW} = 3.5$ and $c_{LL} = 3.6$.

Equations (24) to (26) give the streamwise (or horizontal) flux, i.e., the mass flux of sand particles moving in saltation, crossing a vertical plane with 1 m width and infinitely high, with units $(kg\,m^{-1}s^{-1})$. The three models consider the horizontal flux as being proportional to the third power of u_*. In order to compute the vertical displacement of each cell, in each time step, the vertical flux (Q_{salt}), or emission rate, with units $(kg\,m^{-2}s^{-1})$, has to be obtained. The vertical flux is assumed to be a fraction of the horizontal flux, q_{salt}, as considered in, e.g., [35–37]. The ratio (q_{salt}/Q_{salt}) has units of length, and assuming saturated conditions for the horizontal flux, such a length is taken equal to the mean jump length of saltation (L_{salt}) [38], given by [39]:

$$L_{salt} = 1091.5 \left(\nu^2/g\right)^{1/3} (u_* - u_{*t,salt})/\sqrt{g d^p} \tag{27}$$

where ν is the fluid kinematic viscosity. The vertical flux due to saltation is then equal to:

$$Q_{salt} = \frac{q_{salt}}{L_{salt}} \tag{28}$$

The assumption of saturated conditions might be questioned because it is not fulfilled in the lower part of the windward slope, as discussed in [40] and [41]. However, at that location, u_* is lower than $u_{*t,salt}$ (as will be discussed in Sect. 6) and, therefore, no erosion occurs due to saltation. The above mentioned assumption is thus locally irrelevant.

In Eqs. (24) to (27), the threshold value, $u_{*t,salt}$, is given by [42]:

$$u_{*t,salt} = A_B \sqrt{(\rho^p/\rho)\, g d^p} \times \sqrt{\psi} \tag{29}$$

where the coefficient A_B is equal to 0.1 [5], for $d^p \geq 100\,\mu m$, and the correction function ψ takes into consideration the possible existence of a non-zero local ground slope angle, θ:

$$\psi = \cos\theta + \frac{\sin\theta}{\tan\beta} \tag{30}$$

In the previous expression, β is the angle of repose ($\beta = 33°$, according to Iversen and Rasmussen [42]).

The ejection velocity is randomly chosen for each particle saltation trajectory, based upon a normal distribution with mean value, $\bar{u}_e^p$, and standard deviation, $u_e'^p$, equal to [43]:

$$\bar{u}_e^p = 0.6u_* \quad u_e'^p = 0.5\bar{u}_e^p \tag{31}$$

Similarly, the angle of ejection (referred to the local ground orientation) is also randomly defined for each particle saltation trajectory, based on a normal distribution with mean value, $\bar{\alpha}_e^p$, and standard deviation, $\alpha_e'^p$, equal to [43]:

$$\bar{\alpha}_e^p = 35^o \quad \alpha_e'^p = 0.1\bar{\alpha}_e^p \tag{32}$$

In turn, the mass flux of erosion due to creeping, q_{creep}, is currently considered in the literature to be related to the saltation mass flux. According to Wang and Zheng [18], the following relation applies:

$$q_{creep} = \alpha_{cr1} \frac{\sqrt{g d^p}}{u_*} q_{salt} \tag{33}$$

where the factor α_{cr1} is empirically defined and will be specified later. Similarly to saltation, the creeping phenomenon is also associated to the local value of the friction velocity, u_*. In the present work, the corresponding threshold value, $u_{*t,creep}$, below which no creeping occurs, is proposed to be given by:

$$u_{*t,creep} = \alpha_{cr2} u_{*t,salt} \tag{34}$$

where the empirical factor α_{cr2} is also defined later.

The length (in the main wind direction) of each saltation trajectory, l_{salt}, is directly determined by its Lagrangian tracking, through integration of Eqs. (21) and (23). This procedure allows the direct determination of the deposition location for each saltation trajectory. An equivalent procedure is not available to predict the length of each particle trajectory due to creeping, l_{creep}. To overcome this difficulty, a formulation proposed by Andreotti et al. [38] was adapted to the present conditions, thus yielding:

$$l_{creep} = 0.5\lambda_{cr} \frac{u_*^2}{\mu_f g} \tag{35}$$

where μ_f is a coefficient of dynamic friction ($\mu_f = 0.4$, following Shao [44]) and λ_{cr} is an additional coefficient which value will be specified later.

In the global simulation procedure, particle trajectories are calculated assuming permanent regime to hold. Solid material pertaining to the Eulerian ground surface control volume (CV) that contains the point of injection of trajectory j is continuously eroded, during the whole period of calculation of the particulate phase, Δt. The amount of eroded material is thus directly proportional to Δt. If A^e denotes a characteristic area of the CV that contains the ejection point of a saltation trajectory, then the vertical (z) coordinate of the central node of that Eulerian CV will diminish by an amount of:

$$\Delta h^e = \frac{(Q_{salt})_j \Delta t}{\rho^p A^e} \tag{36}$$

Correspondingly, material deposition occurs at the ground surface CV where j saltation trajectory ends. The central node of that incidence CV is thus vertically raised by an amount given by:

$$\Delta h^i = \frac{(Q_{salt})_j \Delta t}{\rho^p A^i} \tag{37}$$

where A^i stands for a characteristic area of that incidence CV. If deposition creates a local slope angle larger than the angle of repose, β, then "avalanche" occurs: the excess solid material slides around until a lesser slope is attained.

Ground deformation due to creeping erosion is treated in exactly the same way.

The global, two-phase calculation procedure is implemented as follows:

(i) The fluid flow phase is first calculated, ignoring the presence of particles.

(ii) The results thus obtained for the continuous phase are then frozen. For each CV of the ground surface, a comparison is established between the local actual and threshold friction velocities, in order to select the particle ejection points, and the calculation for the dispersed phase is launched. As already stated, this Lagrangian component of the calculation procedure is performed assuming stationary conditions to hold: each trajectory, j, corresponds to a given amount of particles per unit time, which are continuously ejected from the same ejection location. Particle ejection lasts for a pre-established time duration, Δt, which is common to all trajectories.

(iii) Following the completion of all particle trajectories, corresponding to a time duration Δt, the new ground configuration is calculated, as a cumulative result of erosion and deposition effects (see Eqs. (36) and (37), respectively). The whole Eulerian grid is then redefined, adapting itself to the newly calculated ground form.

(iv) The calculation procedure returns to step (i) and continues, until a preset time limit $t = \sum_i \Delta t$ has been attained. In short, the total physical time, t, during which all erosion and deposition phenomena actually occur, is artificially divided into a number of parcels, i, each lasting for a time equal to Δt, at the end of which a partial adjustment of the ground form takes place. Global precision of the whole procedure is ensured by using conveniently small values of Δt.

The empirically based coefficients that are used in Eqs. (24) to (27) and (33) to (35) were essentially established by the original authors for flat, horizontal ground configurations and specific sand granulometry. This is rather different from the geometry used in the present study, in which the initial, non-disturbed dune surface has a sinusoidal type form. As a consequence, those empirical coefficients need to be calibrated for the present situation, as reported in Sect. 5.
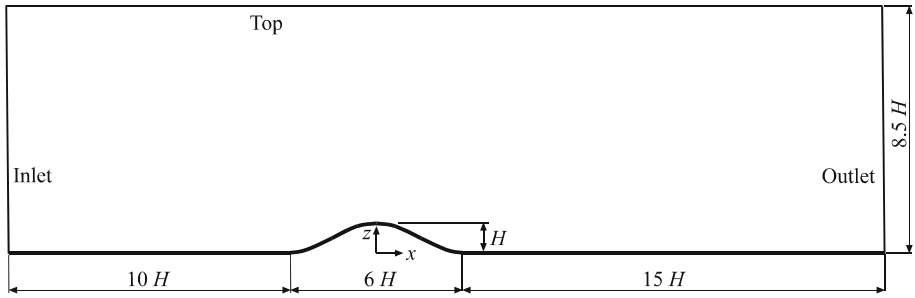
Fig. 1 Simulation domain: dimensions and boundaries

3 Case study description

Although the whole calculation procedure described in the preceding sections is able to simulate three-dimensional two-phase flows, the physical situation actually studied in the present work is essentially two-dimensional.

3.1 Problem statement and simulation characterization

The geometry adopted in this work reproduces the experimental conditions of Ferreira and Fino [19]. The longitudinal initial profile of the dune is given by the following equation:

$$z = \frac{H}{2}\left[1 + \sin\left(\pi \times \left\{\frac{x}{L/2} + \frac{1}{2}\right\}\right)\right] \qquad (38)$$

where L and H stand for the initial length ($L = 360\,\text{mm}$), and height ($H = 60\,\text{mm}$) of the dune, respectively. The x coordinate is aligned with the undisturbed flow ($x = 0$ at the central axis of the dune), and z is the vertical coordinate. Figure 1 depicts the calculation domain, along with the geometric dimensions and identification of the boundaries. Domain extension and dune location were adjusted so as to ensure that nearly zero gradient conditions are achieved at the inlet, outlet and top boundaries.

Based on the wind tunnel measurement data, a fully developed turbulent velocity profile was assigned at the inlet boundary, according to the following equation:

$$\frac{u}{U_\infty} = \left(\frac{z}{\delta}\right)^n \qquad (39)$$

where u is the local streamwise velocity, $U_\infty = 9.1\,m/s$ is the undisturbed velocity, $\delta = 0.1\,m$ is the boundary layer height and $n = 0.11$ characterizes the profile shape. Regarding turbulence specification, values of 10 % turbulence intensity and 0.02 m turbulence length scale were assigned at this boundary.

Zero gradient (parabolic) conditions for all the variables were set at the outlet. At the domain top a slip boundary was considered. In the dune region, a uniform roughness length, $z_0 = 0.05\,\text{mm}$ (corresponding to $d^p/10$), was set to the ground surface.

3.2 Time and space grid independence

The computational mesh was generated using a simple algebraic method, with constant spacing along the streamwise direction. A uniform vertical distance of 0.1 mm (between the ground and the first CV centre) was used at the bottom boundary, for a total of 31 nodes along
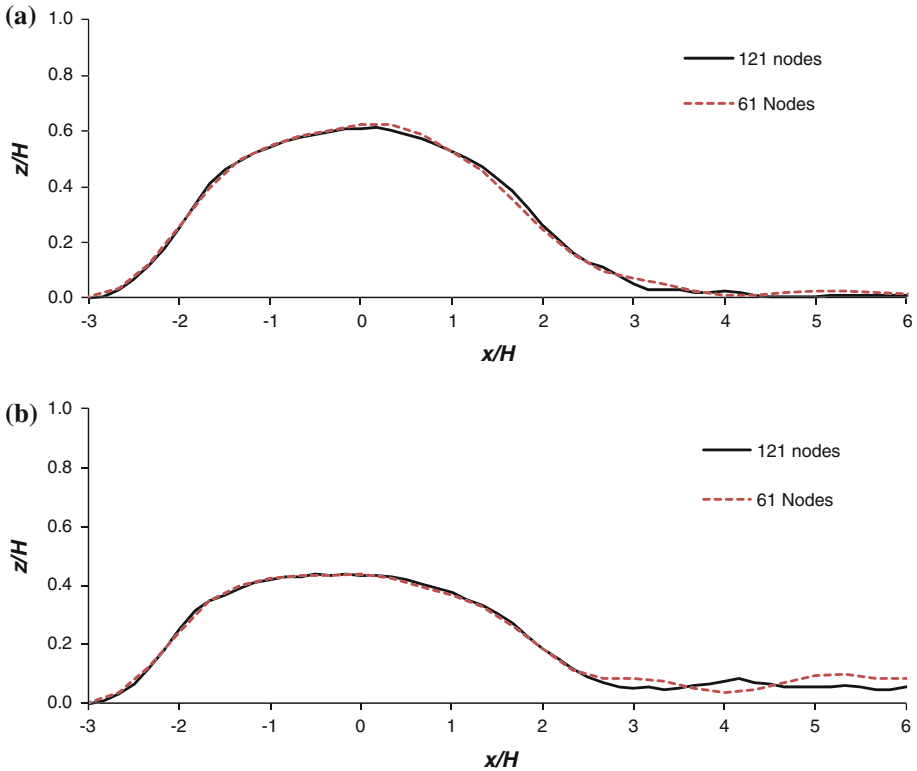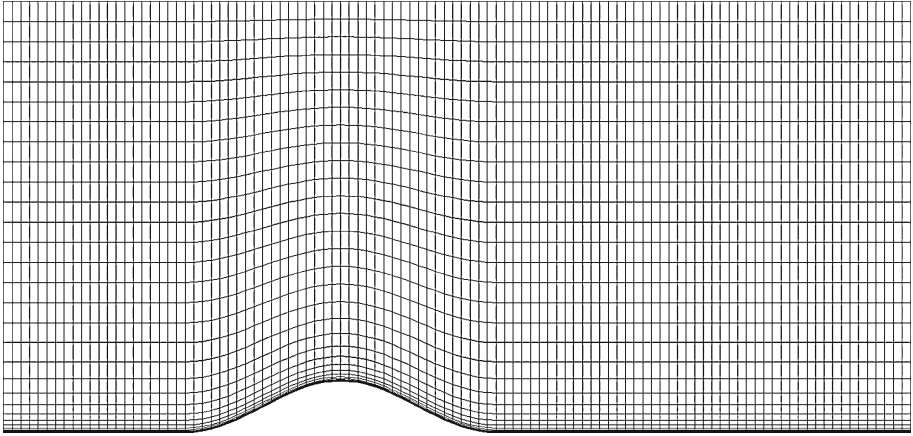
Fig. 2 Dependence of results with the mesh refinement in the streamwise direction: **a** $t = 4$ min; **b** $t = 8$ min. Vertical scale is about $3\times$ the horizontal scale

the vertical direction, distributed with a variable expansion factor. Increasing the number of vertical levels did not have a noticeable effect in the results. Dependency of results with the longitudinal mesh resolution is presented in Fig. 2, for two time levels. One may observe that, although small, differences in the results obtained with these two meshes are more noticeable at the downstream region for $t = 8$ min. For the remaining parts of the dune, both results are mostly undistinguishable. Following these results, the 121 nodes configuration was adopted for the simulations presented next. The corresponding mesh layout may be observed in Fig. 3.

For temporal discretization studies, the time step for the global time marching procedure, Δt, was set equal to 1 s, 4s and 10 s. Figure 4 presents the dune shape obtained in the simulations using these time step values, at two instants. Differences in the results are only noticeable for $t = 8$ min and are visually enhanced by the exaggerated vertical scale. Following these observations, the $\Delta t = 4\,s$ option was selected for the remaining simulations.

4 Results and discussion

Qualitative comparison of simulation results and experimental data was done by plotting the surface shape obtained through both methods. For a quantitative evaluation of the relative performance of the tested models, the root mean square of the dune surface vertical coordinate deviation to the experimental data was used. This is defined as follows:

Fig. 3 Final mesh used in the simulations (only the region around the non-eroded dune is shown)
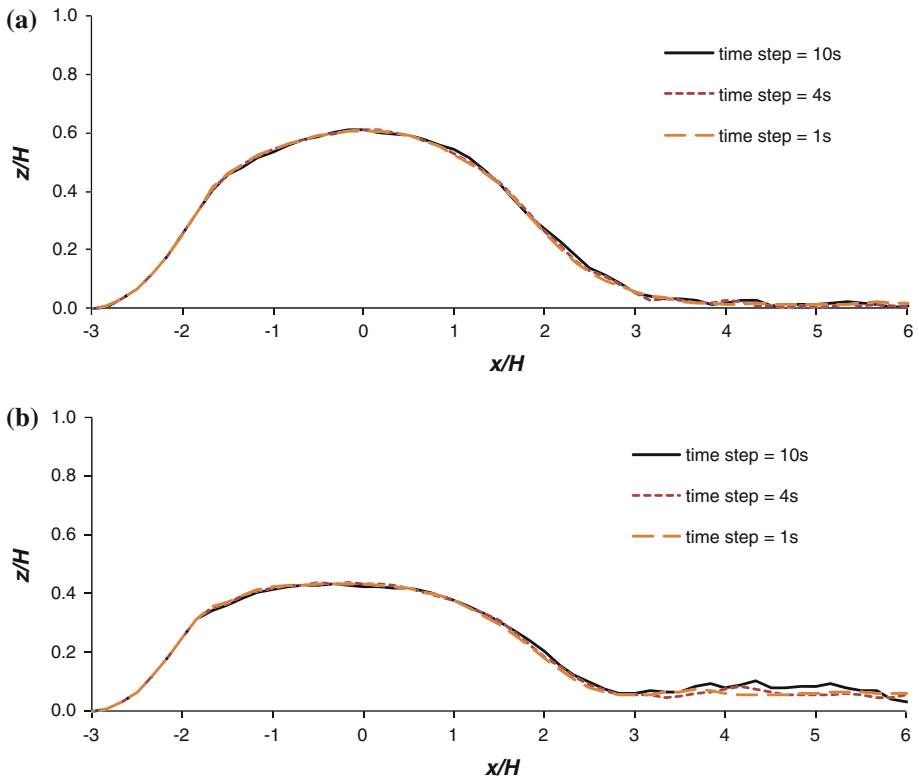
Fig. 4 Dependence of results with the time step Δt: **a** $t = 4$ min; **b** $t = 8$ min. Vertical scale is about $3\times$ the horizontal scale

(a)

(b)
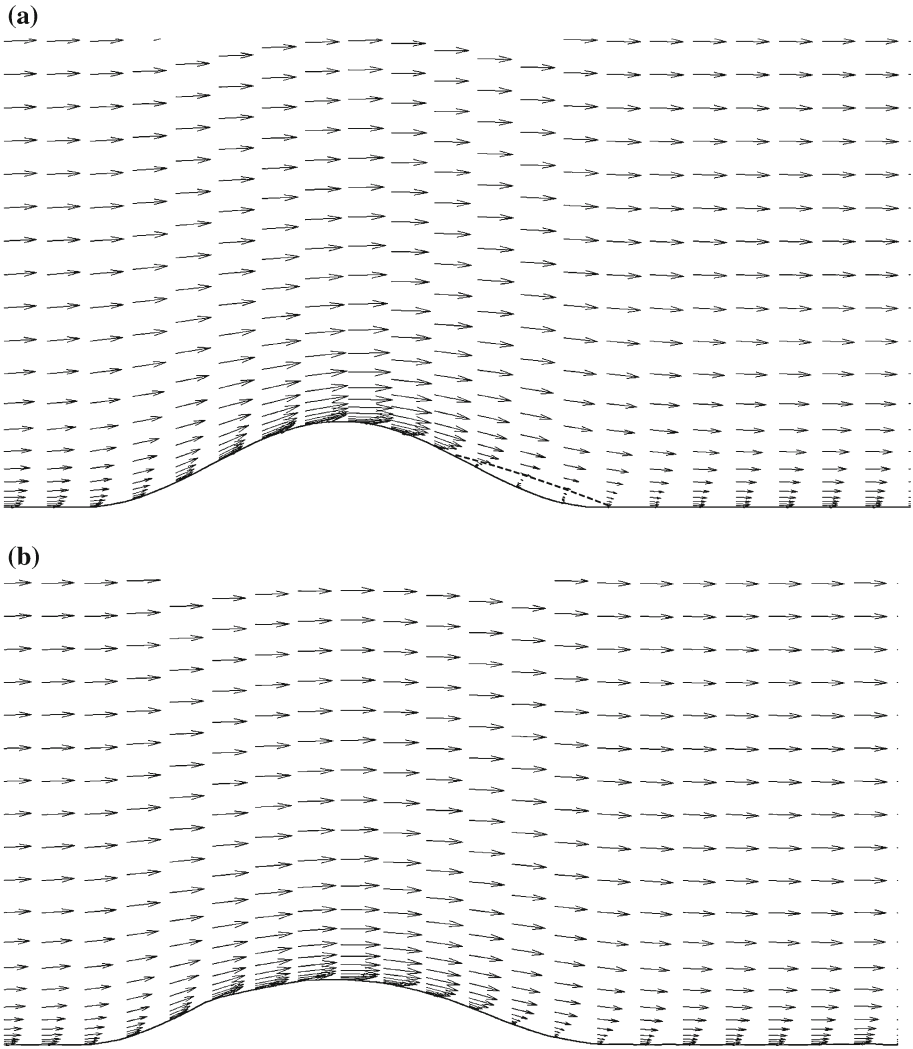
Fig. 5 Vectorial representation of the air flow velocity field: **a** $t = 0$ min; **b** $t = 2$ min. For better visualization, vectors are represented every other node along the horizontal direction. The dashed line identifies the recirculation region

$$\sigma_z = \sqrt{\overline{\Delta z_{ij}^2}} \tag{40}$$

where the vertical deviations Δz where taken at all i computational nodes on the sand surface, for the j time instants $t = 2, 4, 6, 8, 12$ min.

4.1 The relative importance of saltation and creeping

Figure 5 shows the distribution of calculated wind velocity vectors for two different instants, namely $t = 0$ and $t = 4$ min. As expected, a recirculation zone is visible for $t = 0$ (just before erosion starts) near the lee side of the dune. Besides, the maximum velocities are initially
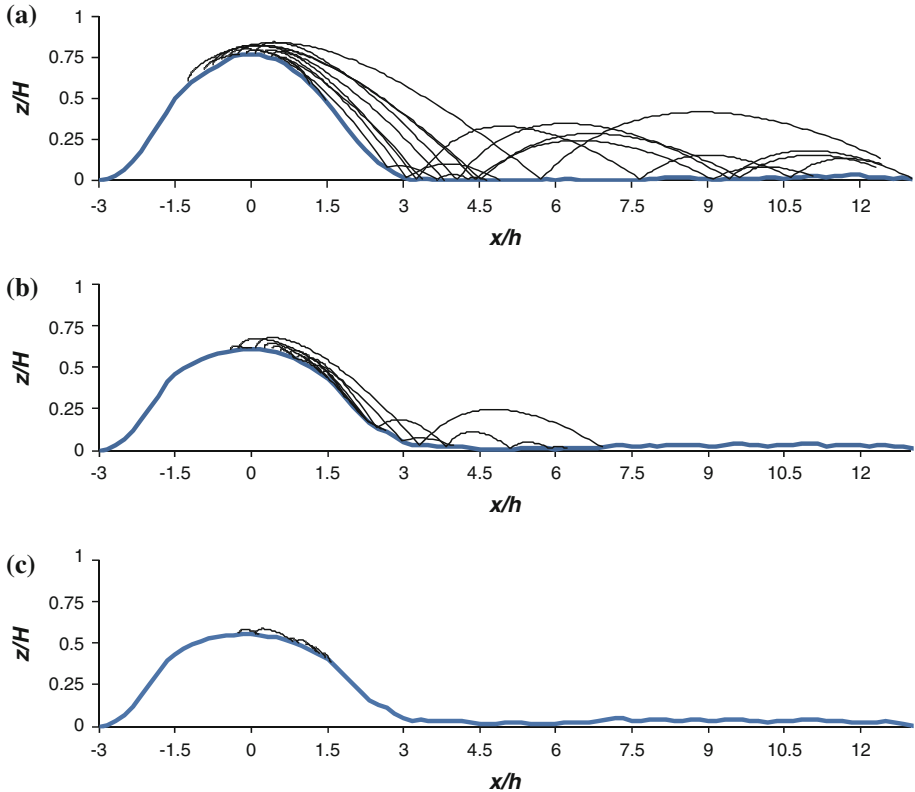
Fig. 6 Trajectories of sand grains from saltation. **a** $t = 2$ min; **b** $t = 4$ min; **b** $t = 5$ min. BG model

located in the close vicinity of the dune top. It is also apparent that these locally high values tend to rapidly decrease as the dune begins to erode.

Correspondingly, the change in shape of the dune leads to a rapid decrease of the shear stress generated by wind at the dune surface. As a consequence, when erosion starts, the local highest values of the surface shear stress drop very rapidly to values lower than the threshold limit for saltation to occur, $u_{*t,salt}$. This can be observed in Fig. 6, where calculated saltation trajectories of sand grains are shown for three instants, namely $t = 2$, 4 and 5 min. In fact, we may notice that, for $t = 5$ min, saltation has practically vanished.

However, experiments show that erosion does keep going on for time levels well beyond $t = 5$ min. This is clear evidence that, for the present dune configuration and sand granulometry, the relative importance of creeping, as compared to saltation, in the global erosion procedure, is much higher than the one predicted in the literature for flat, horizontal initial ground configurations.

The model that is proposed in this study for the whole erosion procedure reflects the relative importance of creeping that is referred to in the preceding paragraphs.

5 Model validation and parameters' fine tuning

Taking the experimental results reported in [19] as the validation reference for the present numerical simulation, several tests were conducted in order to assess the relative performance

of different models, as well as distinct parameter values within those models. Namely, the three saltation BG, KW and LL models represented by Eqs. (24)–(26) were tested, as well as different formulations for the creeping-to-saltation mass flux ratio (represented by α_{cr1} in Eq. (33)), creeping threshold (through α_{cr2} in Eq. (34)) and creeping deposition length (through λ_{cr} in Eq. (35)). An additional function, C_ψ, was defined in order to inhibit creeping flux in regions of the dune surface with positive slope and providing, simultaneously, a rapid transition around zero slope into the "creeping region" for positive slope:

$$C_\psi = \psi^4 \quad \text{if } \theta \geq 0 \tag{41}$$

$$C_\psi = \psi^{0.5} \quad \text{if } \theta < 0 \tag{42}$$

so that: $\alpha_{cr1} = A/C_\psi$, in Eq. (33); $\alpha_{cr2} = BC_\psi$, in Eq. (34); $\lambda_{cr} = C/C_\psi$, in Eq. (35), ψ being given by (30). Here, A, B and C are parameters which values will be fine-tuned below.

5.1 Influence of the saltation model

Temporal evolution of the dune shape is shown in Fig. 7, for instants $t = 4$, 8, and 12 min, using the three aforementioned saltation models BG, KW and LL. As already stated, best fitting (between experiments and CFD predictions) for the three saltation models was achieved by using $c_{BG} = 4.066$, $c_{KW} = 3.5$ and $c_{LL} = 3.6$ in Eqs. (24)–(26). The creeping parameters are kept unchanged. As reported below, they too correspond to the best fitting values, namely $\alpha_{cr1} = 10/C_\psi$, $\alpha_{cr2} = 0.25C_\psi$ and $\lambda_{cr} = 11/C_\psi$. The root mean squares of the vertical deviation values are $\sigma_{BG} = 7.3\%$; $\sigma_{LL} = 11.4\%$; $\sigma_{KW} = 8.5\%$. Closer approximation to experiments was thus obtained with the BG model, which is therefore adopted in the subsequent analysis.

Looking at Fig. 7, it can be seen that, depending on the saltation model, the predicted dune profile varies quite significantly, in particular in the range $0 < x/H < 2$ and at $t = 12$ min (Fig. 7c). A similar trend was observed in the experiments, in the same x/H range, as evidenced by the large dispersion of the experimental data, which is a clear indicator of the high nonlinear nature of the aeolian erosion phenomenon.

At $t = 12$ min, while the LL and KW models suggest a relatively low erosion rate, the BG model yields a considerably large erosion flux leading, by deposition, to the formation, or ejection, of a new dune in the lee side. While the two former models preserve a relatively large slope of the pile's leeward face, the stronger erosion predicted by the BG model leads to the earlier disappearance of the recirculation bubble. This latter model was thus adopted for the subsequent analysis.

5.2 Influence of the creeping coefficient parameter

Several tests were also conducted, aiming at evaluating the sensitivity of the model towards the value of the creeping coefficient parameter, α_{cr1}, defined at the beginning of Sect. 5 as $\alpha_{cr1} = A/C_\psi$. Evidence from experiments showed that the relative influence of creeping in the whole erosion procedure strongly increases for negative slopes ($\theta < 0$) and tends to vanish for positive slopes. This is taken into account in the above mentioned definition of α_{cr1}, as both functions ψ and C_ψ decrease for increasingly negative slopes. As a sample of the sensitivity tests, Fig. 8 shows the time evolution of the dune surface for three instants $t = 4$, 8, and 12 min, using two different approaches: BG1, for which $\alpha_{cr1} = 10/C_\psi$; and BG5, corresponding to $\alpha_{cr1} = 3/C_\psi$. All remaining parameters are kept unchanged, namely $\alpha_{cr2} = 0.25C_\psi$ and $\lambda_{cr} = 11/C_\psi$. Although perfect agreement with experiments is never achieved, BG1 approach always leads to the more favourable comparison, quantified
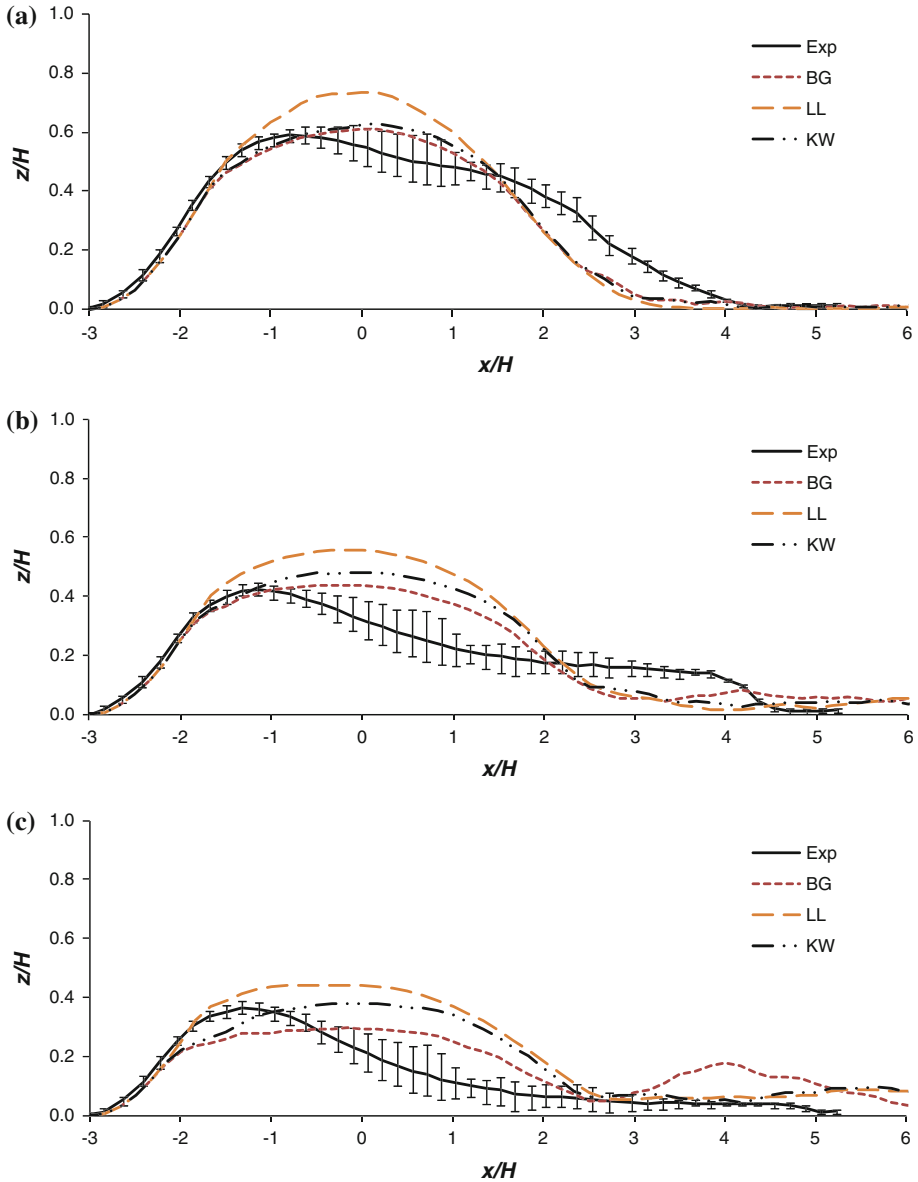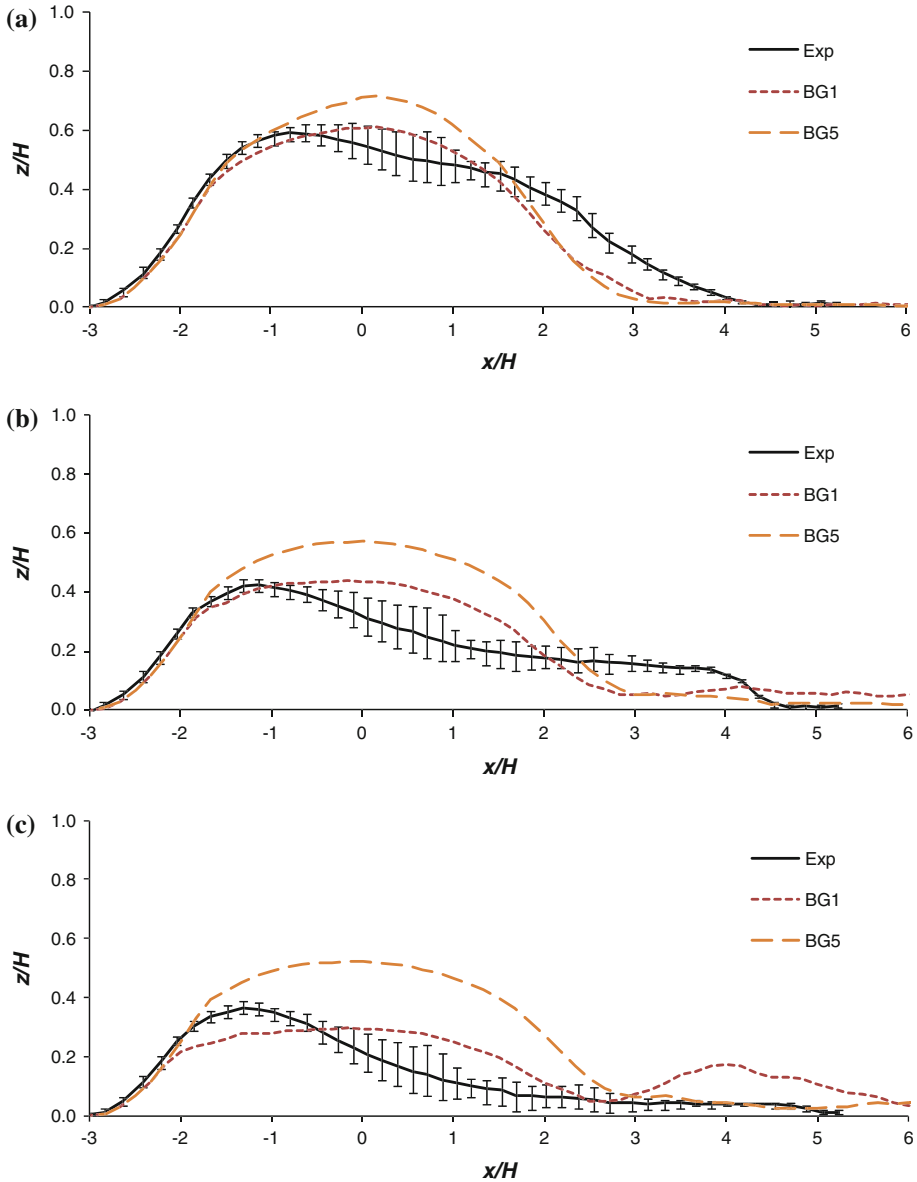
Fig. 7 Dune shape at 3 instants: comparison between different models. **a** $t = 4$ min; **b** $t = 8\,min$; **c** $t = 12$ min. Vertical scale is about $3\times$ the horizontal scale

as $\sigma_{BG1} = 7.3\,\%$; $\sigma_{BG5} = 13.1\,\%$. It is thus chosen for the analysis to be reported in the next paragraphs.

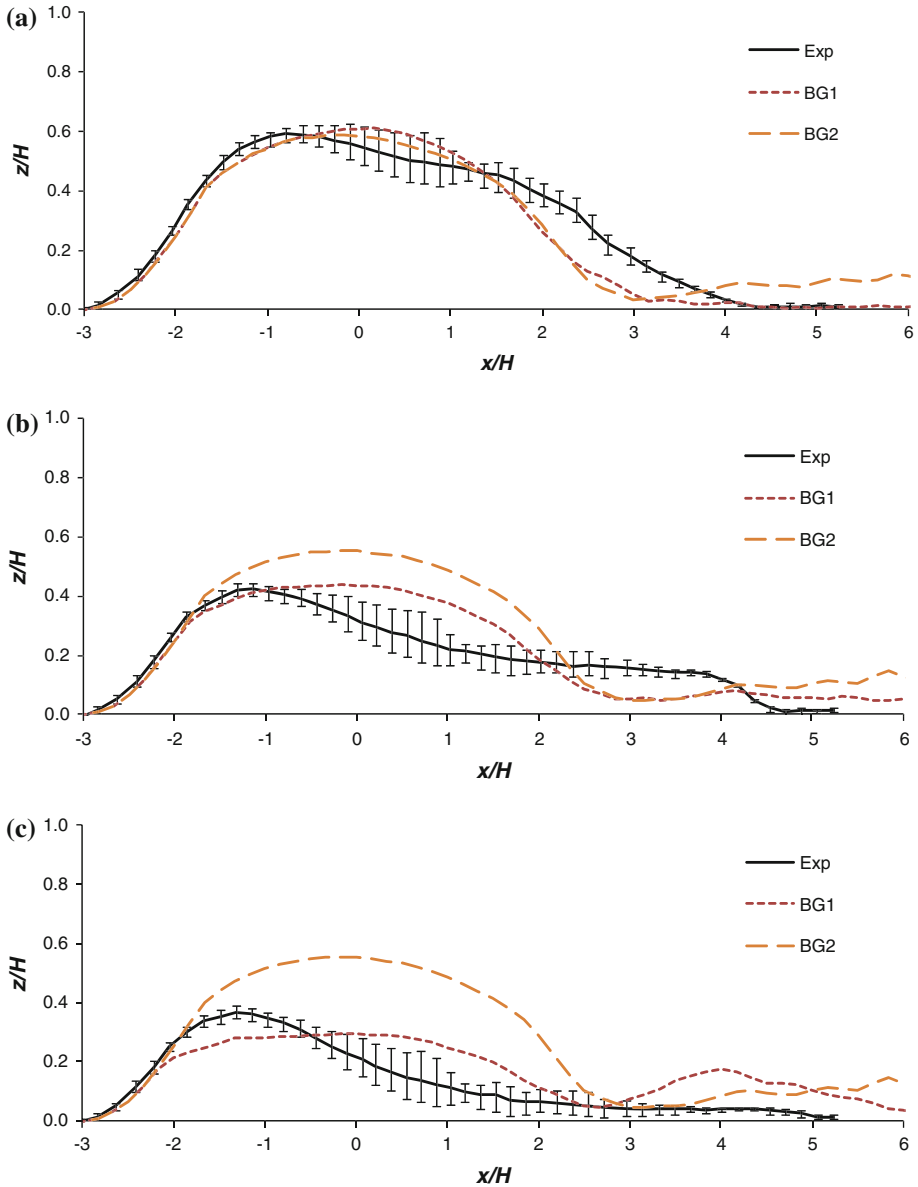### 5.3 Influence of the creeping threshold value

The brief analysis established in Sect. 4.1 clearly shows that dune erosion by creeping does stand for a much longer time than erosion due to saltation. This means that the threshold value

Fig. 8 Dune shape at 3 instants: influence of creeping coefficient. **a** $t = 4$ min; **b** $t = 8$ min; **c** $t = 12$ min. Vertical scale is about $3\times$ the horizontal scale

of surface friction velocity, $u_{*t,creep}$, below which erosion by creeping no longer takes place, is lower than the corresponding threshold value for saltation, $u_{*t,salt}$. Such a feature is taken into account in Eq. (34), as α_{cr2} is there less than unity. Moreover, experimental evidence showed that creeping trigger is clearly favoured by negative slopes. This feature is taken into consideration in the above mentioned definition of the threshold coefficient $\alpha_{cr2} = BC_{\psi}$, as, again, both functions ψ and C_{ψ} decrease for increasingly negative slopes. Several tests

Fig. 9 Dune shape at 3 instants: influence of creeping threshold. **a** $t = 4$ min; **b** $t = 8$ min; **c** $t = 12$ min. Vertical scale is about $3\times$ the horizontal scale

were conducted in order to evaluate the relative influence of parameter α_{cr2}. An illustrative sample is shown in Fig. 9, where the temporal evolution of the dune profile is represented for three instants, namely $t = 4$, 8, and 12 min, using two different approaches: BG1, for which $\alpha_{cr2} = 0.25C_\psi$; and BG2, corresponding to $\alpha_{cr2} = 1.0C_\psi$. All remaining parameters are constant and shared by the different tests, namely $\alpha_{cr1} = 10/C_\psi$ and $\lambda_{cr} = 11/C_\psi$.

Again, agreement with experiments is not entirely satisfactory. Still, BG1 model leads to much better results than model BG2, with $\sigma_{BG1} = 7.3\,\%$ and $\sigma_{BG2} = 12.5\,\%$, and is therefore used in the analysis to follow.

5.4 Influence of the creeping distance parameter

Experiments reported in reference [19] evidenced that distances covered by sand grains along their creeping path significantly increase for larger negative slopes. This is taken into consideration through the definition of the creeping distance parameter, $\lambda_{cr} = C/C_\psi$, that was given at the beginning of Sect. 5, because, as already stated, both functions ψ and C_ψ decrease for increasingly negative slopes. In analogy to the formerly reported parametric tests, numerical experiments were also conducted aiming to assess the relative influence of λ_{cr} upon the whole erosion phenomenon. Sample results are shown in Fig. 10, where the time evolution of the dune surface is depicted for three time levels, $t = 4$, 8, and 12 min, using two different approaches: BG1, for which $\lambda_{cr} = 11/C_\psi$; and BG4, corresponding to $\lambda_{cr} = 6/C_\psi$. All remaining parameters are constant and shared by the different tests, namely: $c_{BG} = 4.066$, $\alpha_{cr1} = 10/C_\psi$ and $\alpha_{cr2} = 0.25C_\psi$.

In summary, the best fitting between experiments and CFD predictions, for all the tests reported in the previous paragraphs, was obtained with model BG1, with $\sigma_{BG1} = 7.3\,\%$ and $\sigma_{BG4} = 9.7\,\%$. This model is therefore adopted for the calculations reported hereafter.

6 Analysis of final results

Following the sensitivity analysis and tuning procedure that is reported in Sect. 5, the following resulting approach was adopted as the global model to simulate dune erosion for the present configuration: (i)—Bagnold model, BG, described in Eq. (24) with $c_{BG} = 4.066$, for the saltation contribution; (ii)—creeping coefficient parameter $\alpha_{cr1} = 10/C_\psi$, in Eq. (33); (iii)—creeping threshold parameter $\alpha_{cr2} = 0.25C_\psi$, in Eq. (34); (iv)—creeping distance parameter $\lambda_{cr} = 11/C_\psi$, in Eq. (35). The C_ψ function has been defined in Eqs. (41) and (42).

In Fig. 11 a comparison is shown between the temporal evolution of the dune profile that was experimentally measured and the corresponding predictions obtained, for the same successive instants, using the present, global erosion model that is recapped in the preceding paragraph. Although full agreement is far from having been achieved, these validation results are actually encouraging, considering the complex, sloppy shape of the initial dune profile. In fact, the calibration of models' empirical constants employed in transport rate models, even for flat surfaces, is still an open topic, as was recently acknowledged by Sherman et al. [45]. Moreover, although the presently studied configuration is essentially two-dimensional, the global model is actually prepared for inclusion of fully three-dimensional ground configurations.

One of the most striking features resulting from this study is the relative importance of the erosion due to creeping, as compared to that resulting from saltation. In the authors' opinion, this is due to the relatively large sand grain diameter value ($d^p = 0.5$ mm), which may be classified as medium-coarse size [46], together with the non-flat nature of the sand surface, which is in clear contrast with the flat, horizontal initial soil configurations, which are central to the great majority of cases reported in the literature.

Figure 12 displays the predicted friction velocity threshold for both erosion modes—saltation, $u_{*t,salt}$ and creeping, $u_{*t,creep}$—as well as the actual surface friction velocity, u_*,
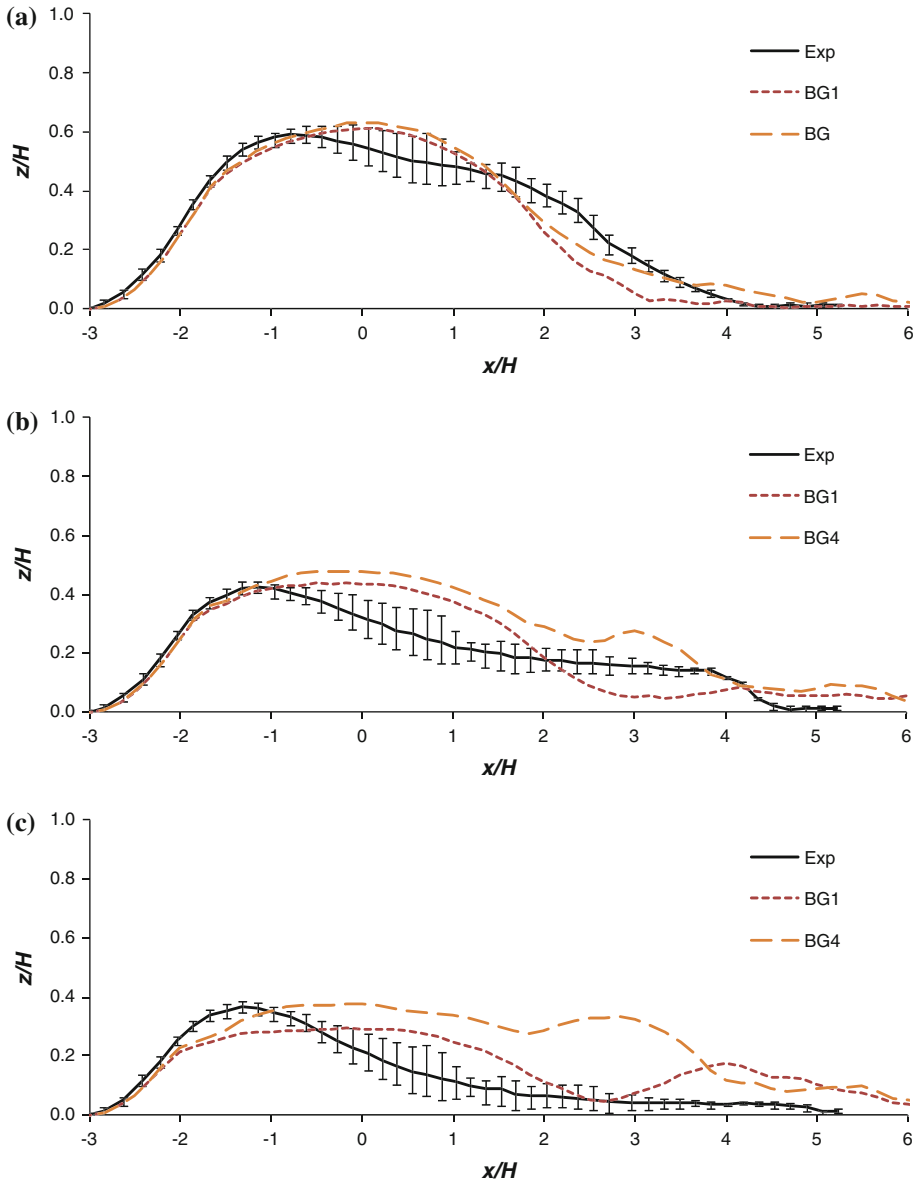
Fig. 10 Dune shape at 3 instants: influence of creeping distance formulation. **a** $t = 4$ min; **b** $t = 8$ min; **c** $t = 12$ min. Vertical scale is about $3\times$ the horizontal scale

along the dune profile. It is clear that saltation only occurs within a localized region (close to the dune crest) for $t = 0$ min and is completely absent for $t = 8$ min (cf. also visualization of trajectories in Fig. 6). In turn, creeping is present in most part of the dune and also downstream, for $t = 8$ min. The apparently surprising behaviour of the threshold lines for $t = 0$ min, showing a localized jump around $x/H = 2$, is actually due to the flow reversal at the recirculation region (cf. Fig. 5a), thus creating a slope discontinuity (it should be recalled
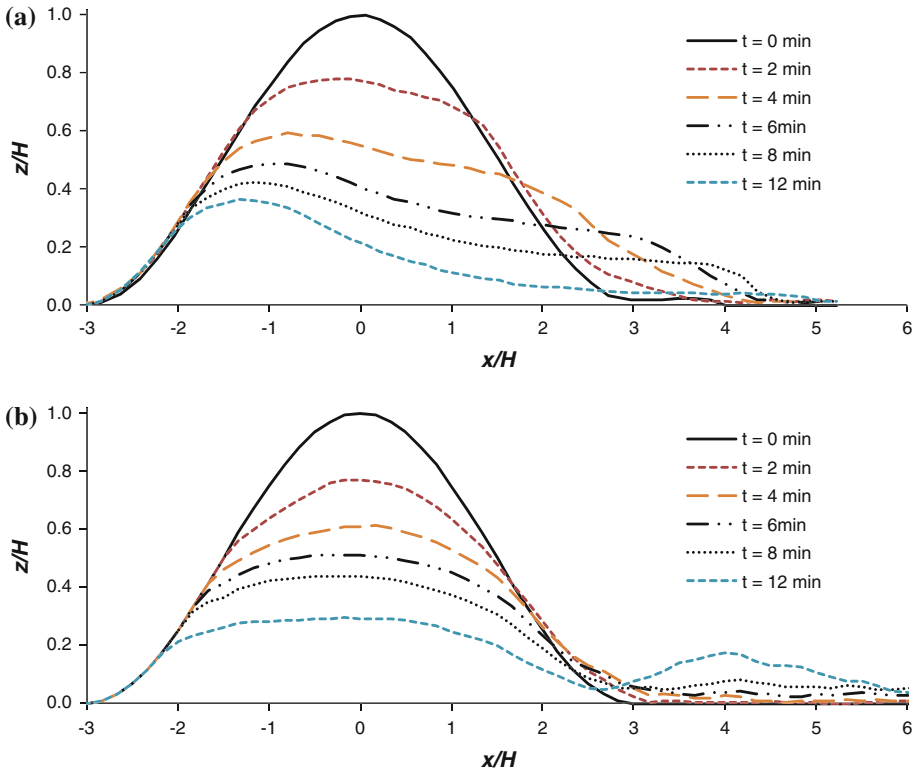
Fig. 11 Dune shape at several instants. **a** Experimental results; **b** Present simulations. Vertical scale is about $3\times$ the horizontal scale

that the slope angle is defined according to the flow direction) and the corresponding effect upon function ψ, defined in Eq. (30).

The time evolution of the relative importance of saltation and creeping sand fluxes leaving the dune surface may be observed in Fig. 13. Erosion by creeping is always present and its total flux is increasing with time due to the sand increasing surface area as a result of the dune extending downstream. The increasingly dune smoothness resulting from the erosion process leads to a decrease in the surface shear stress values, thus inhibiting saltation. After approximately 5 min, shear values fall below the corresponding threshold and erosion by saltation completely vanishes.

7 Conclusions

Erosion is a rather complex phenomenon resulting from the interaction of several mechanisms contributing to the removal of particles from their initial position. The present work describes an innovative numerical method coupling CFD calculations for the fluid flow with modeling of erosion by creeping and saltation. The present numerical method includes Lagrangian tracking of particles as a means of computing saltation length. The aim of this work was also to extend erosion calculations to complex sand surface shapes.

(a)

(b)
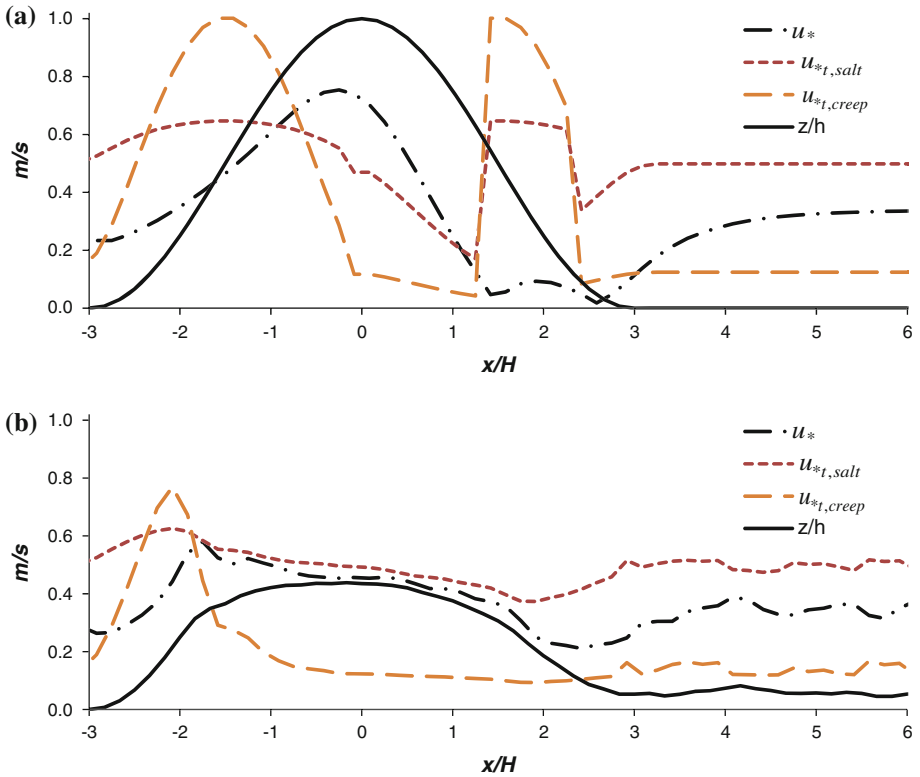
Fig. 12 Local friction velocity and corresponding saltation and creeping thresholds. **a** $t = 0$ min; **b** $t = 8$ min
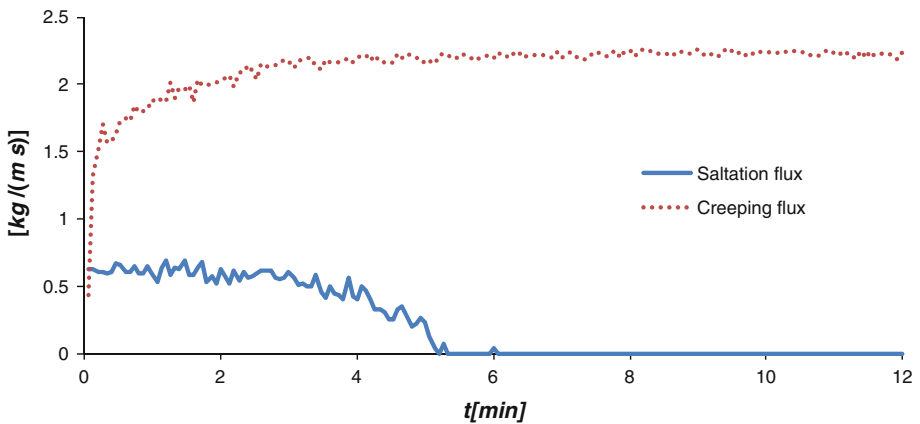
Fig. 13 Total fluxes, per unit width, leaving the dune surface for $-3.0 < x/H < 13$

Comparison of the numerical results with data from wind tunnel experiments allowed a better tuning of coefficients for the creeping-to-saltation flux ratio, creeping threshold, creeping distance and saltation flux model. Although saltation and creeping emission fluxes due to erosion are both functions of the friction velocity, the former depends essentially on the second power of friction velocity, while the later is mostly linear (cf. Eqs. (24)–(26), (27)

and ([33](#)). This feature represents a fundamental difference in the erosion process, especially when the friction velocity is itself dependent on the erosion, as in the present case, where the dune shape is smoothed by erosion.

Reasonable agreement with experiments is only achieved when the creeping mechanism is given a dominant role in the global erosion model. This is actually not surprising, as the grain diameter considered in this work is relatively large. Moreover, the creeping threshold friction velocity showed to be nearly 25 % of the corresponding threshold for saltation, a difference to which the effect of local slope still had to be added through inclusion of function C_ψ, defined in Eqs. ([41](#)) and ([42](#)).

Although being very encouraging, the results obtained in the present study still leave room for improvement, namely through the simulation of two way coupling effects, aiming to take into account the local perturbation of wind flow due to the momentum associated with sand particles. Further testing is also envisaged, including different sand particle diameters and surface topographies, such as a two dunes in tandem, in order to better tune and settle the proposed model.

References

1. Crowe CT, Sommerfeld M, Tsuji Y (1998) Multiphase flows with droplets and particles. CRC Press LLC, London
2. Fan L-S, Zhu C (1998) Principles of gas-solid flows. Cambridge University Press, Cambridge
3. Shao Y (2008) Physics and modelling of wind erosion, 2nd edn. Springer, Montreal
4. Pye K, Tsoar H (2009) Aeolian sand and sand dunes. Springer, Berlin
5. Bagnold RA (1941) The physics of blown sand and desert dunes. Methuen, London (reprinted, (1954) 1960; 2005, by Dover. Mineola, NY)
6. Werner BT (1995) Eolian dunes: computer simulations and attractor interpretation. Geology 23:1107–1110
7. Narteau C, Zhang D, Rozier O, Claudin P (2009) Setting the length and time scales of a cellular automaton dune model from the analysis of superimposed bed forms. J Geophys Res 114(F03006):1–18
8. Barchyn TE, Hugenholtz CH (2011) A new tool for modeling dune field evolution based on an accessible, GUI version of the Werner dune model. Geomorphology 138:415–419
9. Eastwood E, Nield J, Baas A, Kocurek G (2011) Modelling controls on aeolian dune-field pattern evolution. Sedimentology 58:1391–1406
10. Stam JMT (1997) On the modelling of two-dimensional aeolian dunes. Sedimentology 44:127–141
11. Kroy K, Sauermann G, Herrmann H (2002) Minimal model for sand dunes. Phys Rev Lett 88(5):3–6
12. Pischiutta M, Formaggia L, Nobile F (2011) Mathematical modelling for the evolution of aeolian dunes formed by a mixture of sands: entrainment-deposition formulation. Commun Appl Ind Math 2:1–21
13. Exner FM (1925) Über die wechselwirkung zwischen wasser und geschiebe in Flüssen (in German). Sitz Acad Wiss Wien Math Naturwiss Abt. 2a 134:165–203
14. Sauermann G, Kroy K, Herrmann H (2001) Continuum saltation model for sand dunes. Phys Rev E 64(3):1–10
15. Jackson PS, Hunt JCR (1975) Turbulent wind flow over a low hill. Q J R Meteorolog Soc 101:929–955
16. Kawamura R (1951) Study of sand movement by wind. Univ. Tokyo. Rep Inst Sci Technol 5:95–112 (in Japanese)
17. Lettau K, Lettau HH (1978) Experimental and micrometeorological field studies of dune migration. In: Lettau HH, Lettau K (eds) Exploring the world's driest climates. Institute of Environmental Science Report 101, Center for Climatic Research, University of Wisconsin, Madison, WI, USA, pp 110–147
18. Wang Z, Zheng X-J (2004) Theoretical prediction of creep flux in aeolian sand transport. Powder Technol 139:123–128
19. Ferreira AD, Fino MRM (2012) A wind tunnel study of wind erosion and profile reshaping of transverse sand piles in tandem. Geomorphology 139(140):230–241
20. Patankar SV (1980) Numerical heat transfer and fluid flow. Hemisphere Publishing Corporation, Washington DC
21. Launder BE, Spalding DB (1974) The numerical computation of turbulent flows. Comput Meth Appl Mech Eng 3:269–289

22. Cebeci T, Bradshaw P (1997) Momentum transfer in boundary layers. Hemisphere Publishing Corporation, New York
23. Van Doormaal JP, Raithby GD (1984) Enhancements of the simple method for predicting incompressible fluid flows. Numer Heat Transfer 7:147–163
24. Lopes AMG, Sousa ACM, Viegas DX (1995) Numerical simulation of turbulent flow and fire propagation in complex terrain. Numer Heat Transfer, Part A 27:229–253
25. Anderson RS, Haff PK (1988) Simulation of eolian saltation. Science 241:820–823
26. Shao Y, Li A (199) Numerical modelling of saltation in the atmospheric surface layer. Bound-Lay Meteorol 91:199–225
27. Oliveira LA, Costa VAF, Baliga BR (2008) Numerical model for the prediction of dilute three-dimensional, turbulent fluid-particle flows, using a Lagrangian approach for particle tracking and a CVFEM for the carrier phase. Int J Numer Meth Fluids 58:473–491
28. Maxey MR, Riley JJ (1983) Equation of motion for a small rigid sphere in a nonuniform flow. Phys Fluids 26:883–889
29. Wallis GB (1969) One-dimensional two-phase flow. McGraw-Hill, New York
30. Oliveira LA, Costa VAF, Baliga BR (2002) A Lagrangian-Eulerian model of particle dispersion in a turbulent plane mixing layer. Int J Numer Meth Fluids 40:639–653
31. Gosman AD, Ionnides E (1981) Aspects of computer simulation of liquid fuelled combustors. AIAA Paper No 81–0323
32. Dong Z, Liu X, Wang H, Wang X (2003) Aeolian sand transport: a wind tunnel model. Sediment Geol 161:71–83
33. Bagnold RA (1956) The flow of cohesionless grains in fluids. Philos Trans R Soc Lond Ser A 249:235–297
34. Ferreira AD, Farimani A, Sousa ACM (2011) Numerical and experimental analysis of wind erosion on a sinusoidal pile. Environ Fluid Mech 11:167–181
35. Gillete DA, Passi R (1988) Modeling dust emission caused by wind erosion. J Geophys Res 93(D11):14233–14242
36. Marticorena B, Bergametti G (1995) Modeling the atmospheric dust cycle: 1. Design of a soil-derived dust emission scheme. J Geophys Res 100(D8):16415–16430
37. Shao Y (2004) Simplification of a dust emission scheme and comparison with data. J Geophys Res 109(D10):1–6
38. Andreotti B, Claudin P, Douady S (2002) Selection of dune shapes and velocities Part 1: dynamics of sand, wind and barchans. Eur Phys J B 28:321–339
39. Almeida MP, Parteli EJR, Andrade JS, Herrmann HJ (2008) Giant saltation on Mars. Proc Natl Acad Sci USA 105(17):6222–6226
40. Lancaster N, Nickling WG, Neuman CKM, Wyatt VE (1996) Sediment flux and airflow on the stoss slope of a barchan dune. Geomorphology 17:55–62
41. Durán O, Herrmann H (2006) Modelling of saturated sand flux. J Stat Mech: Theory Exp 7:P07011–P07011
42. Iversen JD, Rasmussen KR (1999) The effect of wind speed and bed slope on sand transport. Sedimentology 46:723–731
43. Nalpanis P, Hunt JCR, Barrett CF (1993) Saltating particles over flat beds. J Fluid Mech 251:661–685
44. Shao Y (2007) Physics and Modelling of Wind Erosion, 2nd edn. Springer, Berlin
45. Sherman DJ, Li B, Ellis JE, Farrell EJ, Maia LP, Granja H (2012) Recalibrating aeolian sand transport models. Earth Surf Process Landf. doi:10.1002/esp.3310
46. Wentworth CK (1922) A scale of grade and class terms for clastic sediments. J Geol 30:377–392